mathematics

Article

Structural Optimization and Application Research of Alkali-Activated Slag Ceramsite Compound Insulation Block Based on Finite Element Method

Xiaona Fan, Yu Guo, Qin Zhao and Yiyun Zhu *

Department of Civil Engineering, Xi'an University of Technology, Xi'an 710048, China; 1190711008@stu.xaut.edu.cn (X.F.); 2180721123@stu.xaut.edu.cn (Y.G.); zhaoqin6688@xaut.edu.cn (Q.Z.)
* Correspondence: zyyun@xaut.edu.cn; Tel: +86-138-9180-8287

Abstract: The research and application of new wall materials have been attracting increasing attention owing to the continuous promotion of sustainable development in the building industry. An alkali-activated slag ceramsite compound insulation block (AASCCIB) is used as the research object. Based on the finite element method, the effects of different numbers of hole rows and hole ratios on the thermal and mechanical performances of AASCCIBs are analyzed using ANSYS CFX. On this basis, the AASCCIB with the optimal comprehensive performance is determined by a multi-objective optimization analysis. Finally, the improvement effect of the AASCCIB wall on the indoor thermal environment relative to an ordinary block (OB) wall is quantitatively analyzed using ANSYS CFX. The results show that the von Mises equivalent stress and heat transfer coefficient of the AASCCIB decrease with the increase in the hole ratio when the hole shape and number of hole rows are constant. AASCCIB B_1 has the optimal comprehensive performance among six AASCCIBs, with the heat transfer coefficient and average von Mises equivalent stress of 0.446 W/(m^2·K) and 9.52 MPa, respectively. Compared with the indoor lowest and average temperatures of the building with the OB wall, those of the building with the AASCCIB wall increased by at least 1.39 and 0.82 °C on the winter solstice, respectively. The indoor temperature difference decreased by at least 0.83 °C. In addition, the indoor highest temperature, average temperature, and temperature difference decreased by at least 1.75, 0.79, and 1.89 °C on the summer solstice, respectively.

Keywords: finite element method; alkali-activated slag ceramsite compound insulation block; ANSYS CFX; thermal and mechanical performances; indoor thermal environment

Citation: Fan, X.; Guo, Y.; Zhao, Q.; Zhu, Y. Structural Optimization and Application Research of Alkali-Activated Slag Ceramsite Compound Insulation Block Based on Finite Element Method. *Mathematics* **2021**, *9*, 2488. https://doi.org/10.3390/math9192488

Academic Editor: Yumin Cheng

Received: 05 September 2021
Accepted: 29 September 2021
Published: 4 October 2021

1. Introduction

With the progress of science and technology and improvement in living standards, higher requirements for living conditions have been imposed. Instead of limiting the demand for buildings to shelter from wind, rain, and warmth, people emphasize the need for a comfortable, energy-saving, and environmentally friendly living environment [1,2]. However, improvements in indoor thermal comfort are often accompanied by increases in building energy consumption and environmental pollution [3,4]. It is reported that buildings account for 40% of the total global energy consumption, and this proportion is still increasing [5,6]. In addition, approximately 40% of the total human greenhouse gas emission is attributed to the building industry [7,8]. Therefore, how to achieve improvements in indoor comfort without significantly increasing energy consumption and greenhouse gas emissions is a thorny issue that countries must face and solve.

In China, wall materials account for approximately 70% of housing construction materials. Clay bricks are the predominant wall material. However, it is statistically demonstrated that more than 1 billion cubic meters of arable land and 70 million tons of coal are consumed each year by the production of clay bricks [9]. If the growth of clay brick production is uncontrolled, the contradiction between supply and demand of resources, as well as energy, will become more acute. Obviously, it is required to promote the innovation of wall materials to realize the sustainable development of buildings. The self-insulation block is a new type of wall material [10]. It occupies a large share of the construction market because of its good heat insulation and thermal insulation, lightweight, high strength, long service life, simple construction, etc. [11]. Commonly, cement is chosen as the cementitious material for self-insulation blocks [12]. The production and processing of cement, however, consumes large amounts of energy and emits a lot of greenhouse gases. The production of 1 t of cement requires 5000 MJ of energy and emits 1 t of CO_2 [13]. Thus, the cementitious material alternative to cement is sought.

In recent years, alkali-activated slag cementitious material (AASCM) obtained using slag (industrial waste) attracted increasing attention [11]. Compared to the traditional cement production process, the AASCM production process transfers from "two grindings and one burning" to "one grinding". This reduces the energy consumption and greenhouse gas emissions of cementitious materials in the production process [14,15]. Additionally, AASCM has the advantages of high strength, high-temperature resistance, frost resistance, corrosion resistance, etc. [15]. Evidently, it is important to achieve sustainable development of building materials by choosing AASCM to replace traditional cement.

Ceramsite is a typical representative of artificial light aggregates and new energy-saving building materials [16]. It is obtained by an industrial solid waste via high-temperature calcination. It has the advantages of recycling waste, environmental protection, convenient production, and low price [17]. It also has a low thermal conductivity, high strength, lightweight, high-temperature resistance, acid and alkali resistance, etc. [18]. Considering these excellent characteristics of ceramsite, it can be used as an aggregate in studies on new wall materials.

To sum up, it is an inevitable choice for wall material development in studies on alkali-activated slag ceramsite self-insulation blocks (AASCSIBs). To improve the thermal performance of the alkali-activated slag ceramsite single self-insulation block, the alkali-activated slag ceramsite self-insulation hollow block (AASCSIHB) is generally filled with an insulation material. That is, an alkali-activated slag ceramsite compound insulation block (AASCCIB) is prepared. Therefore, conducting research on AASCCIBs will promote the integrated development of energy efficiency and functionality of buildings.

Nevertheless, there are a few reports on AASCCIBs [11,19] which focus on the preparation and performance of the block. In other words, there are very few studies devoted to the structural optimization and application feasibility of AASCCIBs [19], especially those dedicated to the comprehensive optimization of mechanical and thermal performances and the exploration of the thermal insulation effect. Undoubtedly, the above limitations restrict the application and promotion of AASCCIBs.

The most commonly used research approach in the structural optimization and application effect analysis of blocks is numerical simulation [20–22]. Various numerical analysis methods are used, including the finite difference method (FDM) [23,24], boundary element method (BEM) [25,26], finite volume method (FVM) [27,28], and finite element method (FEM) [29,30]. The FDM is a dominant numerical method for solving the motion of objects in computational fluids. However, it is challenging to solve the boundary conditions using this method. The BEM transforms the solution of the entire domain into a solution on a regional boundary. This numerical method reduces the computational effort, but is inefficient for the computation of the complex-shape flow field. In addition, the method is generally suitable for only solving homogeneous linear problems. The largest advantage of the FVM is that it provides an accurate integral conservation even with coarse meshes. However, the accuracy of the FVM is only second-order. The FEM is a numerical technique used to obtain approximate solutions to boundary value problems of partial differential equations. The basic idea of the method is to discretize the continuous solution domain, i.e., to divide the continuum into a finite number of tiny blocks with regular shapes. The method is not only applicable to complex geometries and boundary conditions, but also has a high computational accuracy and wide applicability. Furthermore, it has a standardized calculation format and can be easily applied programmatically. Thus, the FEM is a powerful, effective, and accurate numerical method.

ANSYS integrates the analyses of structure, fluid, electric, magnetic, and acoustic fields [31]. As far as professional computer-aided engineering software is concerned, ANSYS is the only analysis and design software worldwide that has passed the IS09001 quality certification. Additionally, the advantages of ANSYS are reflected in the broad scope of analysis, powerful coupling analysis functions, and convenient co-simulation platform. ANSYS CFX, a branch of ANSYS, is dedicated to fluid dynamics simulation [31]. Notably, it is the first commercial software in the world to develop and use a fully implicit multigrid coupled solver technique. Moreover, it has advanced algorithms, rich physical models, and accurate calculation results. Considering the above analysis, ANSYS CFX is recommended for the structural optimization and application effect analysis of AASCCIBs.

In summary, this study aims to optimize the structure and analyze the thermal insulation effect of the AASCCIB using the FEM. The specific work is as follows:

- Six types of AASCCIBs with different internal structures are designed based on different numbers of hole rows and hole ratios.
- Based on the FEM, the thermal and mechanical performances of six AASCCIBs are simulated using ANSYS CFX. Moreover, the AASCCIB with the optimal comprehensive performance is determined though a multi-objective optimization analysis.
- The improvement effect of the AASCCIB wall on the indoor thermal environment relative to an ordinary block (OB) wall is quantitatively analyzed using ANSYS CFX.

2. Methods

2.1. Structural Design of AASCCIBs

Based on the literature [32], the dimensions of the selected blocks were length × width × height = 390 mm × 240 mm × 190 mm. Furthermore, because the thermal resistance of a hollow block with a rectangular hole was larger than those of diamond, square, and circle at the same hole ratio [33], the hole shape was rectangular in this study. On this basis, six types of hollow blocks with different internal structures were designed based on different numbers of hole rows and hole ratios. The diagram of the AASCSIHBs is shown in Figure 1.

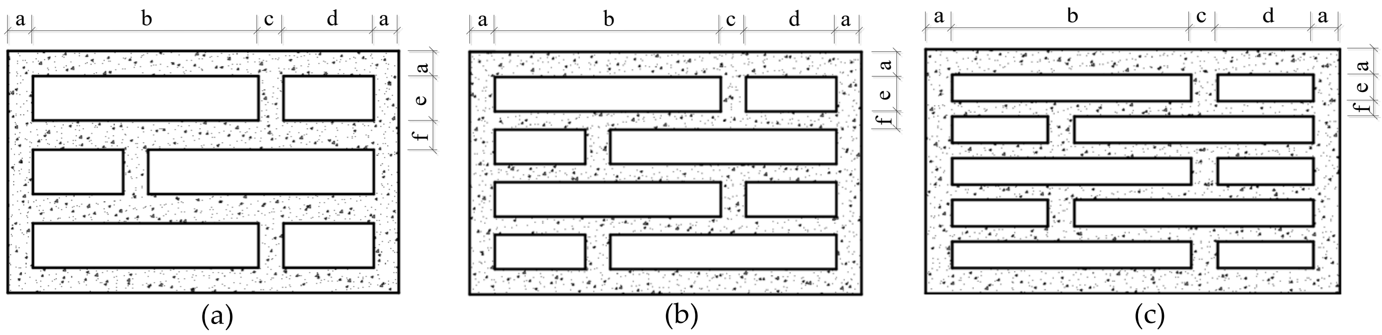

Figure 1. Diagram of AASCSIHBs. (**a**) Three rows of holes; (**b**) Four rows of holes; (**c**) Five rows of holes.

The distance between rows of the rectangular holes was the same. The distance between the rectangular holes parallel to the length direction of the block was referred to as horizontal rib, and the value was *c*. The distance between the rectangular holes perpendicular to the width direction of the block was referred to as vertical rib, with a value of *f*. The length and width of the larger rectangle in each row of the hole were *b* and *e*, respectively. The length and width of the smaller rectangle were denoted by *d* and *e*, respectively. In addition, a was taken as 25 mm according to the reference [32]. The detailed dimensions of the AASCSIHBs are shown in Table 1.

Table 1. Detailed dimensions of AASCSIHBs.

Number	Number of Hole Rows	*a*	*b*	*c*	*d*	*e*	*f*	Hole Ratio /%
A_1	Three rows	25	225	25	90	44	29	44.4
A_2		25	225	25	90	42	32	42.4
B_1	Four rows	25	225	25	90	34	18	45.8
B_2		25	225	25	90	31	22	41.7
C_1	Five rows	25	225	25	90	26	15	43.8
C_2		25	225	25	90	25.2	16	42.9

Note: The hole ratio was the ratio of the hole area to the cross-sectional area of the block.

2.2. Numerical Simulation of Thermal and Mechanical Performances of AASCCIBs

To improve the thermal performance of the block, the holes of the AASCSIHB were filled with an extruded polystyrene (XPS) foam board, which yielded the AASCCIB. Based on the FEM, the thermal and mechanical performances of the six AASCCIBs were numerically analyzed.

2.2.1. Mathematical Model

The heat transfer calculations for this study were performed on a single block wall. In addition, a single block in the wall was selected for the heat transfer analysis of the wall.

According to Fourier's law and energy conservation equation, the differential equation of heat conduction in the three-dimensional (3D) Cartesian coordinates system was established. In the heat transfer analysis, the heat input and output to the differential cube over time $d\tau$ were as follows [34]:

The heat input was:

$$dQ_x = q_x dydz \cdot d\tau ,\ \ dQ_y = q_y dxdz \cdot d\tau ,\ \ dQ_z = q_z dxdy \cdot d\tau \tag{1}$$

The heat output was:

$$dQ_{x+dx} = (q_x + \frac{\partial q_x}{\partial x} dx)dydz \cdot d\tau \tag{2}$$

$$dQ_{y+dy} = (q_y + \frac{\partial q_y}{\partial y} dy)dxdz \cdot d\tau \tag{3}$$

$$dQ_{z+dz} = (q_z + \frac{\partial q_z}{\partial z} dz)dydx \cdot d\tau \tag{4}$$

The net heat between input and output was as follows:

$$\begin{aligned} &\left(dQ_x - dQ_{x+dx}\right) + \left(dQ_y - dQ_{y+dy}\right) + \left(dQ_z - dQ_{z+dz}\right) \\ &= -(\frac{\partial q_x}{\partial x} + \frac{\partial q_y}{\partial y} + \frac{\partial q_z}{\partial z})dxdydz \cdot d\tau \end{aligned} \tag{5}$$

According to Fourier's law [35],

$$q_x = -\lambda \frac{\partial T}{\partial x}, \quad q_y = -\lambda \frac{\partial T}{\partial y}, \quad q_z = -\lambda \frac{\partial T}{\partial z} \tag{6}$$

By substituting Equation (6) into Equation (5), we obtained Equation (7).

$$\begin{aligned} &-\left(\frac{\partial q_x}{\partial x} + \frac{\partial q_y}{\partial y} + \frac{\partial q_z}{\partial z}\right) dxdydz \cdot d\tau \\ &= \left[\frac{\partial}{\partial x}\left(\lambda \frac{\partial T}{\partial x}\right) + \frac{\partial}{\partial y}\left(\lambda \frac{\partial T}{\partial y}\right) + \frac{\partial}{\partial z}\left(\lambda \frac{\partial T}{\partial z}\right)\right] dxdydz \cdot d\tau \end{aligned} \tag{7}$$

The heat generation of the infinitesimal cube over time $d\tau$ was $q_v d_x d_y d_z \cdot d\tau$ [34].

The increment in the thermodynamic internal energy of the microelement over time $d\tau$ was $\rho c \frac{\partial T}{\partial \tau} \cdot d_x d_y \cdot d\tau$ [34].

According to the law of conservation of energy,

$$\begin{aligned} &\left[\frac{\partial}{\partial x}\left(\lambda \frac{\partial T}{\partial x}\right) + \frac{\partial}{\partial y}\left(\lambda \frac{\partial T}{\partial y}\right) + \frac{\partial}{\partial z}\left(\lambda \frac{\partial T}{\partial z}\right)\right] dxdydz \cdot d\tau + q_v d_x d_y d_z \cdot d_\tau \\ &= \rho c \frac{\partial T}{\partial \tau} \cdot d_x d_y d_z \cdot d_\tau \end{aligned} \tag{8}$$

$$\text{i.e., } \left[\frac{\partial}{\partial x}\left(\lambda \frac{\partial T}{\partial x}\right) + \frac{\partial}{\partial y}\left(\lambda \frac{\partial T}{\partial y}\right) + \frac{\partial}{\partial z}\left(\lambda \frac{\partial T}{\partial z}\right)\right] + q_v = \rho c \frac{\partial T}{\partial \tau} \tag{9}$$

Considering that ρ, p, c, and λ are constants, as well as there being no internal heat source inside the wall, Equation (9) was simplified to Equation (10). That is, the mathematical model was established.

$$\frac{\partial^2 T}{\partial x^2} + \frac{\partial^2 T}{\partial y^2} + \frac{\partial^2 T}{\partial z^2} = 0 \tag{10}$$

where *T* is the temperature, °C. *x*, *y*, and *z* are the 3D Cartesian system coordinates.

The mechanical performance in this study was analyzed using the constitutive model with the von Mises yield criterion. The core concept of this criterion was that when the second invariant ($J_{2'}$) of the stress deviation tensor of a point in a stressed object reached a constant value, the point entered the plastic state.

This criterion can be expressed by the principal stresses [36]:

$$J_{2'} = \left[(\sigma_1 - \sigma_2)^2 + (\sigma_2 - \sigma_3)^2 + (\sigma_3 - \sigma_1)^2\right] = c \tag{11}$$

A unidirectional tensile experiment showed that $c = \frac{\sigma_s^{\ 2}}{3}$ [36].

According to a pure shear experiment, it was found that $c = K^2$ [36].

Thus, the von Mises yielding criterion in the principal coordinate system was:

$$(\sigma_1 - \sigma_2)^2 + (\sigma_2 - \sigma_3)^2 + (\sigma_3 - \sigma_1)^2 = 2\sigma_s^{\ 2} = 6K^2 \tag{12}$$

In addition, according to the von Mises yield criterion, the material began to yield when the equivalent force reached a constant value, which can be expressed as [37]:

$$\overline{\sigma} = \frac{1}{\sqrt{2}}\sqrt{(\sigma_x - \sigma_y)^2 + (\sigma_y - \sigma_x)^2 + (\sigma_z - \sigma_x)^2 + 6(\tau_{xy}{}^2 + \tau_{yz}{}^2 + \tau_{zx}{}^2)} = \sigma_s \quad (13)$$

where $\overline{\sigma}$ is the equivalent stress (Pa), σ_i (σ_{ii}) is the normal stress (Pa), σ_s is the yield point, τ_{ij} is the shear stress (Pa), *K* is the shear yield strength (Pa), The first and second subscripts of the stress components indicated the normal direction of the action plane and direction of the stress action, respectively.

2.2.2. Development of the Finite Element Model

1. Basic assumptions and geometric model

The following assumptions were used before the thermal model was developed:

1) The block performs a one-dimensional heat transfer.
2) The temperatures on both sides of the block are constant.
3) The main material of block and the filling material are closely connected. The material performances do not vary with the thermal environment.

Using $\mathrm{AASCCIB\ B_1}$ as an example, a geometric model for the thermal analysis was developed (Figure 2).

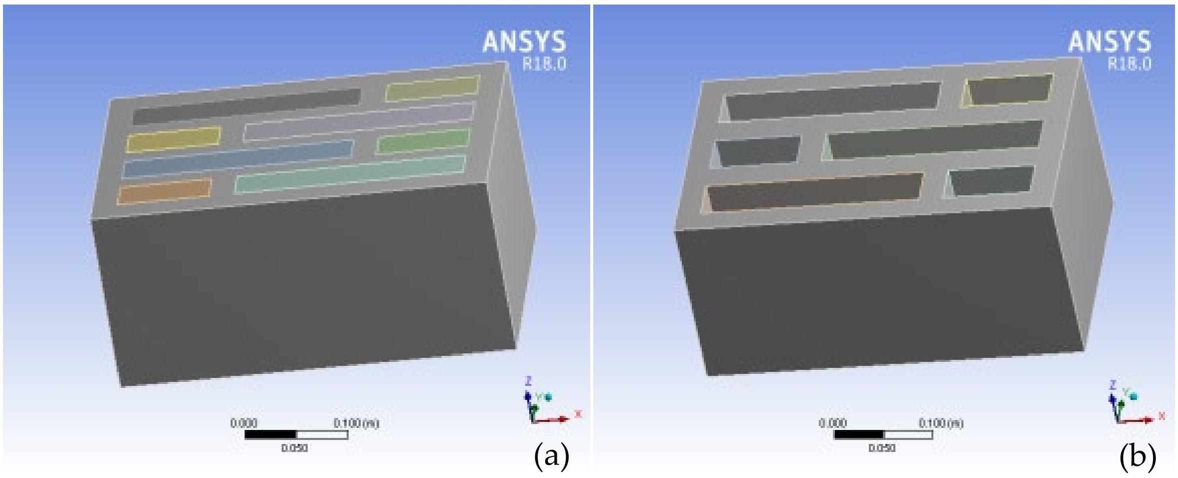

Figure 2. (**a**) Geometric model for the thermal analysis; (**b**) geometric model for the mechanical analysis.

The thermal insulation material (XPS) inside the holes of self-insulation hollow blocks had a small influence on the overall mechanical performances of the compound insulated block. Therefore, the self-insulation hollow block was selected instead of the compound insulation block for the mechanical performance analysis. The geometric model for the mechanical analysis was developed using $\mathrm{AASCSIHB\ A_1}$ as an example (Figure 2).

2. Mesh division

The mesh division of the developed geometric models was conducted. The results are shown in Figure 3.

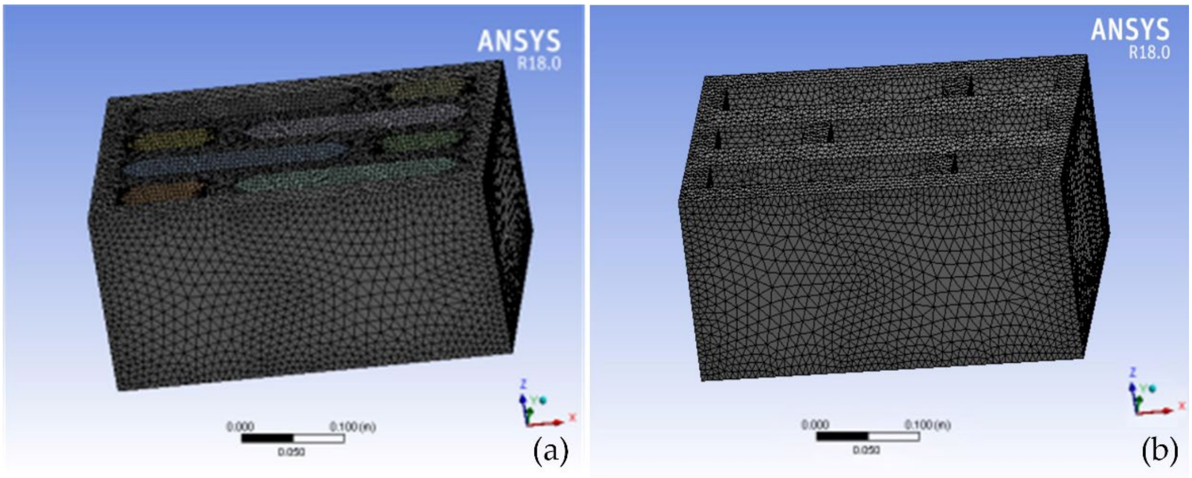

Figure 3. (**a**) Mesh model for the thermal analysis; (**b**) mesh model for the mechanical analysis.

3. Material parameter and boundary condition setting

The physical parameters of the AASCCIB are listed in Table 2. The block surfaces in contact with air were subjected to convective heat transfer boundary conditions (the third boundary condition). The other surfaces of the block were set with adiabatic boundary conditions. The expressions for the third boundary condition were as follows [38]:

$$-\lambda_1 \frac{\partial t}{\partial y}\bigg|_{y=0} = h_i\left(t_{i1} - t_{e1}\right) \tag{14}$$

$$-\lambda_1 \frac{\partial t}{\partial y}\bigg|_{y=h_i} = h_i\left(t_{e2} - t_{i2}\right) \tag{15}$$

$$-\lambda_2 \frac{\partial t}{\partial y}\bigg|_{y=0} = h_e\left(t_{i1} - t_{e1}\right) \tag{16}$$

$$-\lambda_2 \frac{\partial t}{\partial y}\bigg|_{y=h_e} = h_e\left(t_{i1} - t_{i2}\right) \tag{17}$$

where λ_1 and λ_2 are the thermal conductivities of the hollow block and air layer, respectively (W/(m·K)). h_i is the internal surface coefficient of heat transfer with a value of 8.7 W/(m^2·K) [39], h_e is the external surface coefficient of heat transfer with a value of 23.0 W/(m^2·K) [39], t_{i1} is the indoor air temperature of 281.15 K [40]. t_{i2} is the outdoor air temperature of 276.25 K [41], and t_{e1} and t_{e2} are the temperatures of the internal and external surfaces of the wall, respectively(K).

Table 2. Physical parameters of the AASCCIB.

Note	Thermal Conductivity W/(m·K)	Density kg/m^3	Specific Heat Capacity J/(kg·K)	Elastic Modulus MPa	Poisson's Ratio
Shell of AASCSIHB	0.35	1600	1.05	27920	0.2
XPS	0.03	35	1.38	/	/

In the mechanical analysis, a static analysis was used to inform the effect of geometric nonlinearity. All degrees of freedom at the bottom of the finite element model were constrained, and a uniform load (P) of 10 MPa was applied to the upper surface of the model (Figure 4).

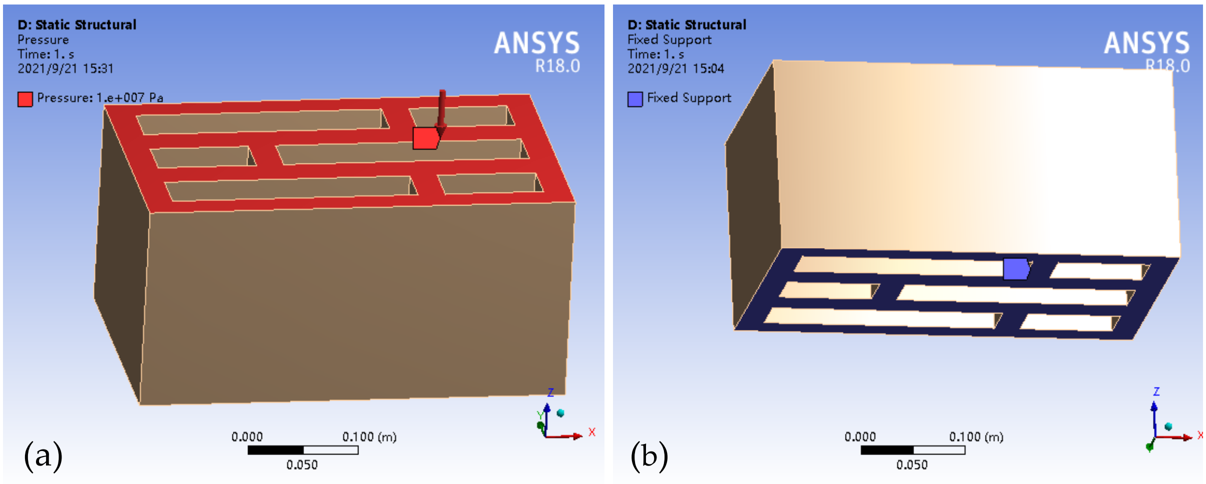

Figure 4. (**a**) Load on the upper surface of the model; (**b**) constraint on the bottom of the model.

2.3. Multi-Objective Optimization of AASCCIBs

2.3.1. Multi-Objective Optimization Method

In this study, the heat transfer coefficient, equivalent stress, and hole ratio represented the thermal, mechanical, and economic performances, respectively. Thermal, mechanical, and economic performances were included in the comprehensive performance. To obtain the AASCCIB with the optimal comprehensive performance, multi-objective optimization was conducted on the compound insulation blocks with different internal structures. The function expression of the weighted summation method was as follows [42]:

$$Max\left[f(x)\right]=\sum_{i=1}^{m}\omega_i f_i(x) \tag{18}$$

where *f(x)* is the objective function, ω_i is the weight coefficient, and $f_i(x)$ is the subobjective function.

2.3.2. Calculation of the Weight Coefficient

The weight coefficients of the block were calculated using a hierarchical analysis. According to the relative importance, weights were assigned to each influencing factor (heat transfer coefficient, equivalent stress, and porosity). In addition, a scale of 1 to 9 was used for importance comparisons of pairwise factors (Table 3). The elements were compared to each other to obtain the judgment matrix *A*, as shown in Formula (19) [43]:

Table 3. Scale values.

Comparison of the importance of factor *i* and factor *j*		Scale (a_{ij})
i and *j* are equally important		1
i is more important than *j*	Gradual increase	3
		5
		7
		9
The median value of two adjacent scales		2, 4, 6, 8

$$A=\left(a_{ij}\right)_{n\times n} \tag{19}$$

where A is the judgment matrix and a_{ij} is the scale.

The maximum eigenvalue of the judgment matrix was calculated, and then a consistency test was performed. The Formulas were as follows [43]:

$$Ax = \lambda_{\max} x \tag{20}$$

$$CI = \frac{\lambda_{\max} - n}{n-1} \tag{21}$$

$$CR = \frac{CI}{RI} \tag{22}$$

where CI is the consistency index, RI is the average consistency index, $\lambda_{\max}$ is the maximum eigenvalue, n is the order of the judgment matrix, and CR is the consistency ratio.

The elements of the matrix A were normalized to obtain the matrix γ. The rows of the matrix γ were summed to obtain the column matrix W. Finally, the matrix W was normalized to obtain the ranking weight vector ω. That is, the percentages of thermal, mechanical, and economic performances that affected the comprehensive performance of the blocks were obtained.

2.3.3. Factor Normalization

The units, sizes, and orders of magnitude of the influencing factors were not consistent, which did not help evaluate the comprehensive performance of the blocks. Therefore, it was necessary to standardize the influencing factors using a normalization method. The calculation Formula for the normalization method was as follows [44]:

$$y_i = x_i \Big/ \sum_{i=1}^{n} x_i \tag{23}$$

where y_i is the dimensionless constant, and $\sum_{i=1}^{n} y_i$ is equal to 1 [44].

2.4. Influence of AASCCIB Wall on the Indoor Thermal Environment

Through the ANSYS CFX simulation, the improvement effect of the AASCCIB wall on the indoor thermal environment relative to the OB wall was informed.

This study considered rural buildings in Southern Shaanxi, China, as the simulation object. The main reason was that Southern Shaanxi, China, is located in the zone of hot-summer and cold-winter, where it is hot in summer and wet with cold in winter. Moreover, the region is close to severe-cold and cold zones, where the average daily temperature reaches about −10 °C in winter [45]. Obviously, the indoor thermal environment of rural buildings in this region needs to be improved urgently. Based on the above analysis, this study took rural buildings in Southern Shaanxi, China, as the simulation object.

2.4.1. Mathematical Model

According to Section 2.1, the 3D unsteady differential equation for heat conduction in the Cartesian coordinate system was as follows:

$$\left[\frac{\partial}{\partial x}(\lambda_x \frac{\partial T}{\partial x}) + \frac{\partial}{\partial y}(\lambda_y \frac{\partial T}{\partial y}) + \frac{\partial}{\partial z}(\lambda_z \frac{\partial T}{\partial z})\right] + q_v = \rho c \frac{\partial T}{\partial \tau} \tag{24}$$

This equation had to be solved in domain Ω. The boundary conditions for this domain were as follows [46]:

$$T = \overline{T} \text{ (On the } \Gamma_1 \text{ boundary)} \tag{25}$$

$$\lambda_x \frac{\partial T}{\partial x} n_x + \lambda_y \frac{\partial T}{\partial y} n_y + \lambda_z \frac{\partial T}{\partial z} n_z = q \quad \text{(On the } \Gamma_2 \text{ boundary)} \tag{26}$$

$$\lambda_x \frac{\partial T}{\partial x} n_x + \lambda_y \frac{\partial T}{\partial y} n_y + \lambda_z \frac{\partial T}{\partial z} n_z = h\left(T_a - T\right) \text{ (On the } \Gamma_2 \text{ boundary)} \tag{27}$$

$$\Gamma_1 + \Gamma_2 + \Gamma_3 = \Gamma \tag{28}$$

where ρ is the density (kg/m³), c is the specific heat capacity (W/(kg·K), τ is the time (s), q_v is the heat flux (W/m²), *T* is the temperature (°C), λ_i is the thermal conductivity along the *i*-axis direction (W/(m·K), n_i is the cosine of the outer normal of the boundary along the *i*-axis direction. q is the heat flux density on the Γ_2 boundary, (W/m²), $\overline{T}$ is the temperature on the Γ_1 boundary (°C), T_a is the external ambient temperature under natural convection conditions (°C), T_a is the absolute temperature of the boundary layer under forced convection conditions (°C), and Γ is the whole boundary of domain *Ω*.

2.4.2. Development of the Finite Element Model

1. Basic assumptions and geometric models

To simplify the model calculation, the following assumptions were used before modeling:

1) The air in each indoor room is considered as a whole. Its heat transfer mode is natural convection heat transfer.
2) The indoor door is open. The door is half-open.
3) The influence of indoor human activities and electrical appliances on the indoor temperature is ignored.

We conducted a field study on rural buildings in Ankang (climatic conditions and building characteristics were representative of rural regions in Southern Shaanxi [45]) during the period from 2017 to 2019. Based on the field research and reference [40], a representative floor plan for rural buildings in Southern Shaanxi, China, was constructed (Figure 5). Further, the geometric model of the representative building was developed using ANSYS CFX, as shown in Figure 6.

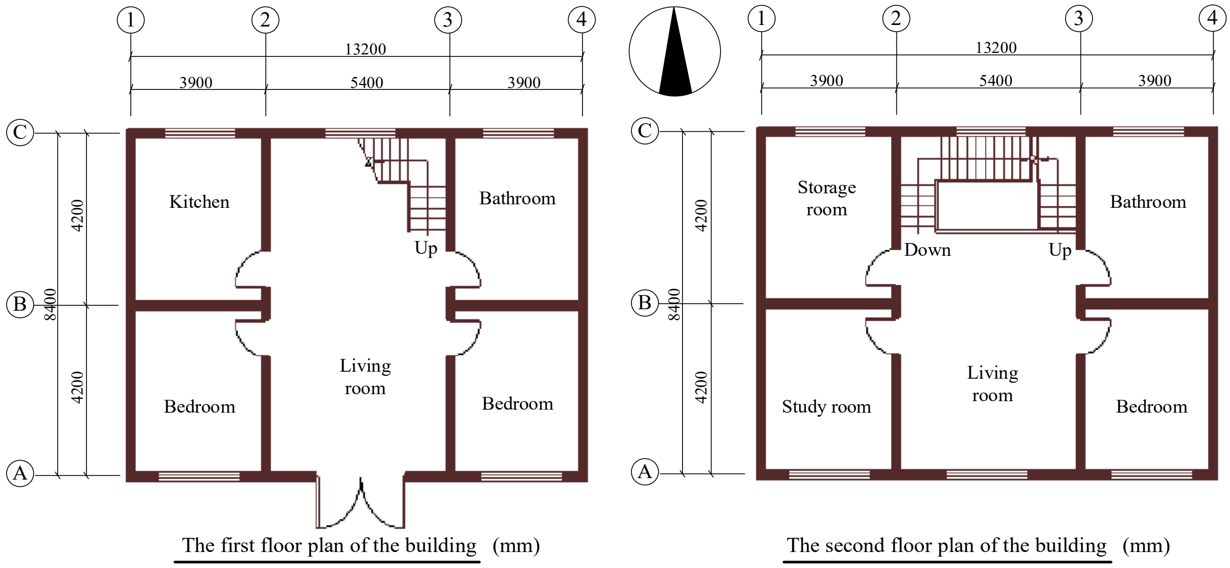

Figure 5. Floor plan of the representative building.

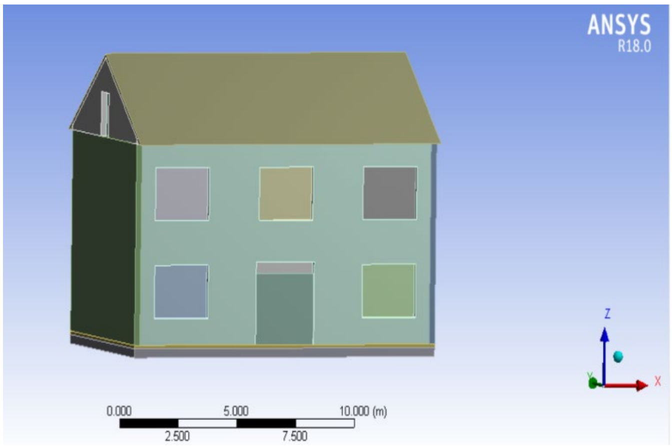

Figure 6. Geometric model of the representative building.

2. Mesh division

In the mesh division, the external surface of the air and internal surface of the external wall, window, door, and roof were mesh-refined. The minimum element size was 0.009 m, and the maximum was 0.967 m. The refined mesh model is illustrated in Figure 7.

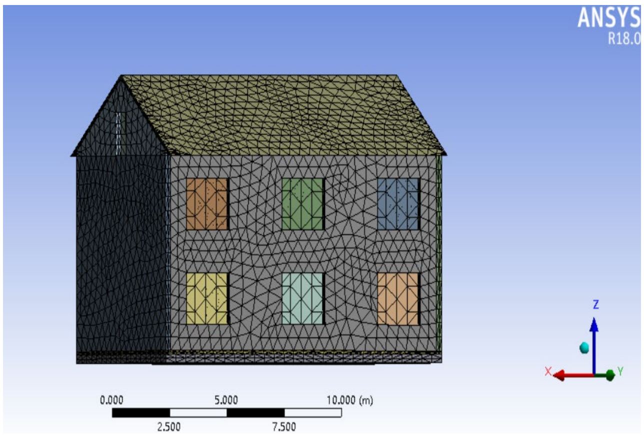

Figure 7. Refined mesh model.

3. Material parameter setting

Based on the field investigation, experimental research, and reference [39], the thermal parameters of the envelope of the building with OB walls and building with AASCCIB walls were obtained (Table 4).

Table 4. Thermal parameters of the envelope.

Item	Material Layer	Thickness mm	Thermal Conductivity W/(m·K)	Density Kg/m³	Specific Heat Capacity J/(kg·K)
External wall (OB wall)	Cement mortar	20	0.93	1800	1050
	Solid clay brick	240	0.81	1800	1050
	Cement mortar	20	0.93	1800	1050
External wall (AASCCIB wall)	Cement mortar	20	0.93	1800	1050
	AASCCIB	240	0.11	867	1050
	Cement mortar	20	0.93	1800	1050
Partition wall	Cement mortar	20	0.93	1800	1050
	Solid clay brick	240	0.81	1800	1050
	Cement mortar	20	0.93	1800	1050
Floor	Cement mortar	20	0.93	1800	1050
	Reinforced concrete	100	1.74	2500	920
	Cement mortar	20	0.93	1800	1050
Roof	Clay tile	20	1.00	2000	800
	Wooden rafter	100	0.17	650	2120
Ground	Pebble concrete	100	1.51	2300	920
	Compacted clay	300	1.16	2000	1010
Window	Single-layer clear glass	3	0.76	2500	840
Door	Wood	150	0.35	500	2510

4. Boundary condition setting

The combined outdoor temperature considered the combined effect of solar radiation and outdoor air temperature on the external envelope of the building. Thus, the comprehensive outdoor temperature was chosen as the boundary condition for the external surface of the wall. Considering that outdoor meteorological parameters generally vary periodically, the comprehensive outdoor temperature was expressed as a sine or cosine function. Further, the comprehensive outdoor temperature was fitted as a periodic sine or cosine function by Fourier series expansion [45]. In addition, the initial temperature of the indoor air body was set to 278.6 K, and the initial temperature of the external surface of the wall was set to 277.1 K in the simulation.

$$t_z(\tau) = A_o + \sum_{n=1}^{\infty} A_n \sin(n\omega\tau + \phi_n) \tag{29}$$

where A_o is the zero-order outdoor disturbance (°C), A_n is the amplitude of the external disturbance of the n-th sine wave (°C), nw is the frequency of the external disturbance of the n-th sine wave, $nw = 2\pi\ n/T$ (rad), φ_n is the initial phase of the external disturbance of the n-th sine wave (rad). T is the period of the function (h), and n is the order of the harmonic.

Formula (29) was expanded by the sine, which yielded Formula (30).

$$t_z(\tau) = A_o + \sum_{n=1}^{\infty} \left[A_n \sin(n\omega\tau + \phi_n) + A_n \cos(n\omega\tau + \phi_n) \right] \tag{30}$$

Assuming that $\dfrac{a_0}{2} = A_0$, $a_n = A_n \sin\varphi_n$, and $b_n = A_n \cos\varphi_n$,

$$t_z(\tau) = \frac{a_0}{2} + \sum_{n=1}^{\infty}\left[a_n \cos(n\omega\tau) + b_n \sin(n\omega\tau)\right] \tag{31}$$

In addition, φ_n was determined by a_n and b_n,

$$b_n > 0 \text{ and } a_n > 0,\ \varphi_n = \arctan\left(\frac{a_n}{b_n}\right) \tag{32}$$

$$b_n > 0 \text{ and } a_n < 0,\ \varphi_n = \arctan\left(\frac{a_n}{b_n}\right) + \frac{\pi}{2} \tag{33}$$

$$b_n < 0,\ \varphi_n = \arctan\left(\frac{a_n}{b_n}\right) + \pi \tag{34}$$

$$b_n < 0 \text{ and } a_n = A_n,\ \varphi_n = \frac{\pi}{2} \tag{35}$$

$$b_n < 0 \text{ and } a_n = -A_n,\ \varphi_n = \frac{3\pi}{2} \tag{36}$$

Because the external disturbance function of the building envelope was extremely complex, the variation in the external disturbance function was expressed by a series of discrete data with equal intervals.

If the basic period interval (0, *T*) was divided into *N* equal parts, the interval only had *N* discrete point values.

$$t_{zj} = t_z(j\Delta\tau),\ j = 0,1,2\ldots N-1,\ \Delta\tau = \frac{T}{N} \tag{37}$$

The rectangular superposition summation method was used to obtain the function expressions of $\dfrac{a_0}{2}$, a_n, and b_n.

$$\frac{a_0}{2} = A_0 = \frac{1}{T}\sum_{j=0}^{N-1} t_{zj}\Delta\tau \tag{38}$$

$$a_n = \frac{2}{T}\sum_{j=0}^{N-1} t_{zj}\cos(n\omega j\Delta\tau)\Delta\tau \tag{39}$$

$$b_n = \frac{2}{T}\sum_{j=0}^{N-1} t_{zj}\sin(n\omega j\Delta\tau)\Delta\tau \tag{40}$$

where *N* is the number of measurement points in a period with a value of 24, *T* is the period, with a value of 24 (h), *n* is the order of the harmonics with a value of 4. *j* is the serial number of the sampled values, and $\Delta\tau$ is the sampling time interval with a value of 1 (h).

Therefore, Formula (31) was transformed into Formula (41).

$$t_z(j\Delta\tau) = A_0 + \sum_{n=1}^{\infty} A_n \sin(n\omega j\Delta\tau + \phi_n) \tag{41}$$

Based on the above analysis, according to the reference [47] and Formula (41), the fourth-order Fourier series expressions for the outdoor comprehensive temperature of different orientations in Ankang region were obtained.

The expressions for the integrated outdoor temperature on the summer solstice were as follows:

$$t_{sa.E(\tau)}=31.2+11.4727\sin(\pi/12+4.1200)+2.5263\sin(\pi/6+2.1621) \\ +1.8760\sin(\pi/4+0.5465)+1.1061\sin(\pi/3+4.33.0) \tag{42}$$

$$t_{sa.S(\tau)}=30.8+11.7485\sin(\pi/12+3.9708)+1.8033\sin(\pi/6+1.5524) \\ +1.0295\sin(\pi/4+0.2122)+0.1788\sin(\pi/3+3.0834) \tag{43}$$

$$t_{sa.W(\tau)}=32.0+14.4902\sin(\pi/12+3.8151)+2.5095\sin(\pi/6+6.1048) \\ +2.4431\sin(\pi/4+0.9260)+1.3697\sin(\pi/3+2.9265) \tag{44}$$

$$t_{sa.N(\tau)}=30.0+11.0814\sin(\pi/12+3.9156)+1.8842\sin(\pi/6+1.2830) \\ +0.4152\sin(\pi/4+0.4529)+0.2020\sin(\pi/3+3.7802) \tag{45}$$

The expressions for the integrated outdoor temperature on the winter solstice were as follows:

$$t_{sa.E(\tau)}=3.5+4.8927\sin(\pi/12+3.5682)+1.1911\sin(\pi/6+0.5243) \\ +1.2650\sin(\pi/4+2.9131)+0.4420\sin(\pi/3+2.5141) \tag{46}$$

$$t_{sa.S(\tau)}=4.7+7.0167\sin(\pi/12+3.7357)+3.0627\sin(\pi/6+0.3954) \\ +2.5353\sin(\pi/4+2.8359)+0.4178\sin(\pi/3+4.3601) \tag{47}$$

$$t_{sa.W(\tau)}=4.1+6.2322\sin(\pi/12+3.0653)+2.3717\sin(\pi/6+0.1049) \\ +2.2533\sin(\pi/4+2.5014)+0.9370\sin(\pi/3+3.8372) \tag{48}$$

$$t_{sa.N(\tau)}=3.4+4.8795\sin\left(\pi/12+3.5414\right)+1.2075\sin\left(\pi/6+0.4287\right) \\ +1.3490\sin\left(\pi/4+2.8836\right)+0.3785\sin\left(\pi/3+2.4847\right) \tag{49}$$

5. Validation of the model

The correctness of the model was verified to ensure that the simulation results were accurate. The measured data were compared to simulated data. The measured data were the indoor temperatures of a representative rural building in Ankang, Southern Shaanxi, China. The results are presented in Figure 8. Each temperature value in the Figure is the average temperature of the room.

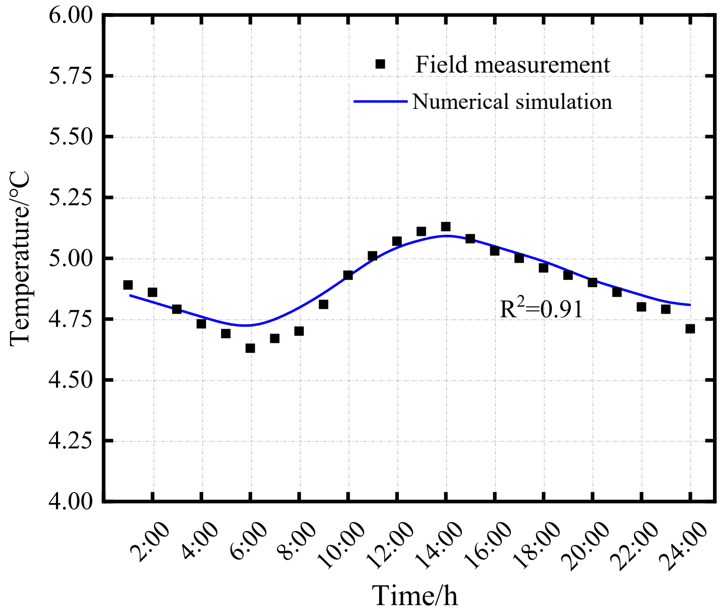

Figure 8. Comparison of measured and simulation results.

Figure 8 shows that the measured temperature was highly consistent with the simulation temperature. The R-squared between the measured and simulated temperatures was 0.91. At the same time, it was found that there was a small deviation between the simulated temperature and measured temperature. This deviation mainly originated from the simplifications and assumptions in modeling and accuracy error of the test instrument. Therefore, it was effective to use ANSYS CFX software to develop a finite element model of the building.

3. Results and Analysis

3.1. Analysis of Thermal and Mechanical Performances of AASCCIBs

Through the simulation by ANSYS CFX, the effects of the different numbers of holes and hole ratios on the thermal and mechanical performances of AASCCIBs were evaluated.

3.1.1. Thermal Performances

Contour plots of temperature and heat flux for the AASCCIB are presented in Figure 9 (for AASCCIB B_1 as an example).

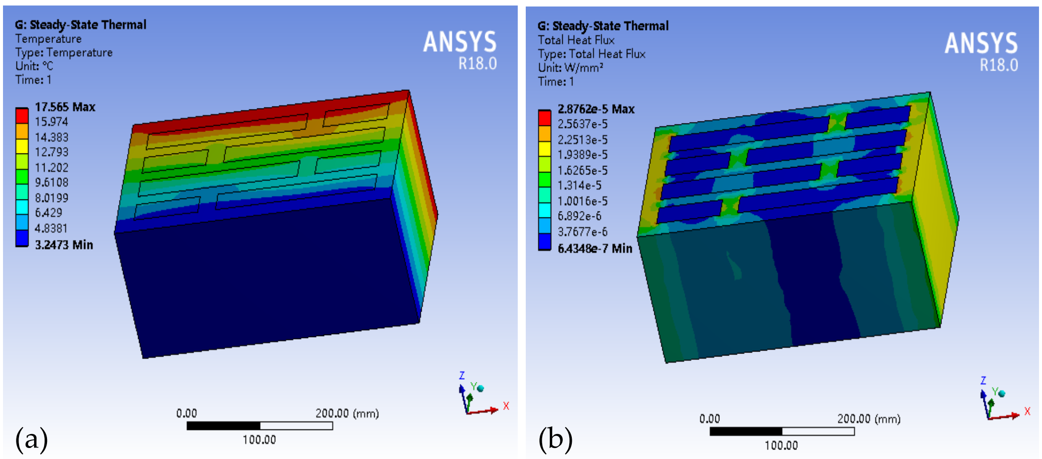

Figure 9. (**a**) Temperature contour plot; (**b**) heat flux contour plot.

Figure 9a shows that the temperature contour plot of the AASCCIB obeyed the fundamental law of heat transfer. The temperature decreased step-by-step from indoor to outdoor along the *Y* direction. As shown in Figure 9b, there was a concentration of heat flux at the vertical ribs, which could easily produce the thermal bridge effect. The main reason was that the heat transfer coefficient of the vertical ribs was larger than that of the other parts, which led to a quick heat transfer from the vertical rib of the block.

In addition, the temperature difference and heat flux intensity on both sides of the flat wall of the AASCCIB were obtained by numerical simulations. Furthermore, the heat transfer coefficient of the AASCCIBs was obtained by Formula (50) [48]. The results are listed in Table 5.

$$K = \frac{q}{\Delta t} \tag{50}$$

where K is the heat transfer coefficient (W/(m²·K)), q is the heat flux intensity, (W/m²), and Δt is the temperature difference between the internal and external surfaces of the wall (K).

Table 5. Simulated thermal performances.

Number	Number of Hole Rows	Hole Ratio %	Temperature Difference °C	Heat Flux Intensity W/m²	Heat Transfer Coefficient W/(m²·K)
A_1	Three rows	44.4	13.871	6.360	0.459
A_2		42.4	13.848	6.452	0.466
B_1	Four rows	45.8	13.881	6.185	0.446
B_2		41.7	13.841	6.531	0.472
C_1	Five rows	43.8	13.885	6.163	0.444
C_2		42.9	13.871	6.225	0.449

Table 5 shows that the heat transfer coefficient of the AASCCIB decreased with the increase in the hole ratio when the hole type and number of hole rows were constant. This was because the increased hole ratio led to the increase in filler thickness when the hole shape and number of hole rows were constant. This directly increased the block heat transfer hindrance, thereby decreasing the heat transfer coefficient.

In addition, the simulated heat transfer coefficient was compared to the theoretical values to validate the finite element model.

The theoretical value of the average heat transfer coefficient of the AASCCIB was calculated by Formulas (51) to (55) [39]:

$$R = \frac{d}{\lambda} \tag{51}$$

$$R = R_1 + R_2 + \cdots R_n \tag{52}$$

$$R_0 = R_i + R + R_e \tag{53}$$

$$\overline{R} = \left[\frac{F_0}{F_1 / R_{0,1} + F_2 / R_{0,2} + \cdots F_n / R_{0,n}} - (R_i + R_e) \right] \cdot \varphi \tag{54}$$

$$\overline{K} = \frac{1}{\overline{R}} \tag{55}$$

where R is the thermal resistance of materials ((m²·K)/W), d is the thickness of each layer material (m), λ is the thermal conductivity of each layer material (W/(m·K)), R_0 is the total thermal resistance of the flat wall ((m²·K)/W), R_i is the internal surface resistance of heat transfer with the value of 0.11 (m²·K)/W [39], R_e is the external surface resistance of heat transfer with the value of 0.04 (m²·K)/W [39], $\overline{R}$ is the average heat transfer resistance of the combined flat wall ((m²·K)/W), F_0 is the total heat transfer area perpendicular to the direction of heat flux (m²), F_1, F_2, … F_n is the area of each heat transfer region parallel to the direction of heat flux (m²), $R_{0,1}$, $R_{0,2}$, … $R_{0,n}$ is each heat transfer area parallel to the direction of the heat flux ((m²·K)/W), φ is the correction factor with the value of 0.86 [39], and $\overline{K}$ is the average heat transfer coefficient of the combined wall (W/(m²·K)).

A calculation diagram of the average thermal resistance is shown in Figure 10. A division diagram of the heat transfer channels is shown in Figure 11.

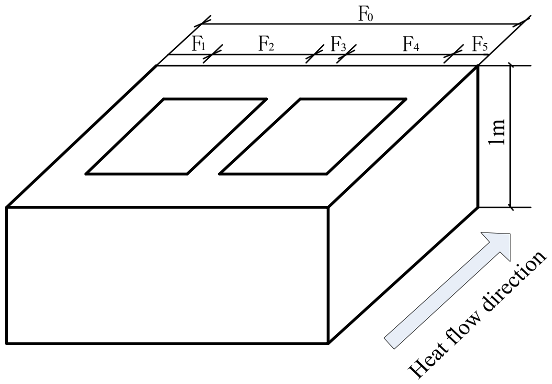

Figure 10. Calculation diagram of the average thermal resistance.

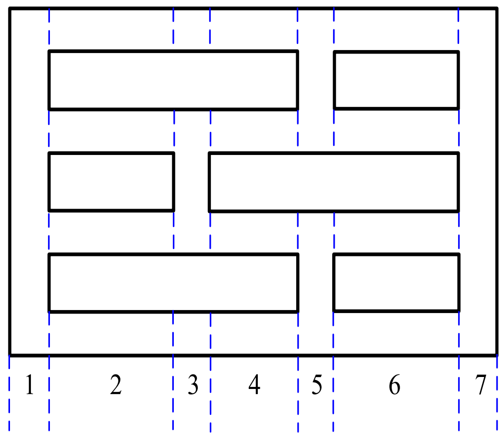

Figure 11. Division diagram of the heat transfer channels.

The average heat transfer coefficient of the AASCCIB was obtained using Formulas (51) to (55).

$$R_{0,1} = \frac{0.24}{0.35} = 0.686 = R_{0,7} \tag{56}$$

$$R_{0,2} = \frac{0.025}{0.35} \times 2 + \frac{0.029}{0.35} \times 2 + \frac{0.044}{0.03} \times 3 = 4.709 = R_{0,4} = R_{0,6} \tag{57}$$

$$R_{0,3} = \frac{0.025}{0.35} \times 2 + \frac{0.029}{0.35} \times 2 + \frac{0.044}{0.03} \times 2 + \frac{0.044}{0.35} = 3.368 \tag{58}$$

$$R_{0,5} = \frac{0.025}{0.35} \times 2 + \frac{0.044}{0.35} \times 2 + \frac{0.044}{0.03} + \frac{0.029}{0.35} \times 2 = 2.027 \tag{59}$$

$$R_1 = R_7 = 0.686 + 0.15 = 0.836 \tag{60}$$

$$R_2 = R_4 = R_6 = 4.709 + 0.15 = 4.859 \tag{61}$$

$$R_3 = 3.518 + 0.15 = 3.518 \tag{62}$$

$$R_5 = 2.027 + 0.15 = 2.177 \tag{63}$$

$$\overline{R} = \left[\frac{F_0}{\frac{F_1}{R_1} + \frac{F_2}{R_2} + \frac{F_3}{R_3} + \frac{F_4}{R_4} + \frac{F_5}{R_5} + \frac{F_6}{R_6} + \frac{F_7}{R_7}} - 0.15 \right] \times 0.86 = 2.30 \tag{64}$$

$$\overline{K} = \frac{1}{\overline{R}} = \frac{1}{2.30} = 0.435 \tag{65}$$

Based on the above calculation, the average heat transfer coefficient of AASCCIB A_1 was 0.435 W/(m²·K). In addition, using the above calculation method, the average heat transfer coefficients of AASCCIBs A_2, B_1, B_2, C_1, and C_2 were 0.444, 0.424, 0.448, 0.434, and 0.442 W/(m²·K).

The simulated and calculated values of the heat transfer coefficient were compared, as shown in Figure 12.

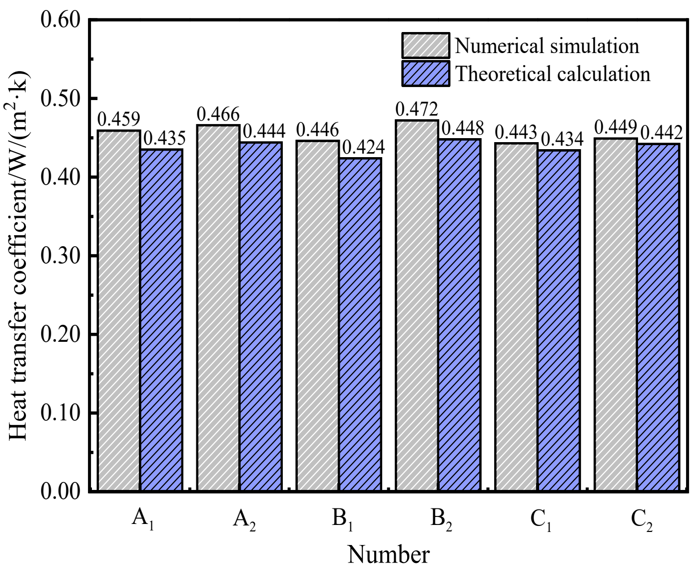

Figure 12. Comparison of simulated and calculated values of heat transfer coefficient.

Figure 12 shows that the calculated and simulated values of the average heat transfer coefficient were almost equal. The relative error of AASCCIB A_1 was the largest (5.5%). The main reason for this error was the series of assumptions in the modeling. Therefore, the finite element building model obtained using ANSYS CFX was considered effective.

3.1.2. Mechanical Performances

Contour plots of deformation and von Mises equivalent stress for AASCSIHB are presented in Figure 13 (for AASCSIHB A_1 as an example). The simulation results of the von Mises equivalent stress of the AASCSIHBs are listed in Table 6.

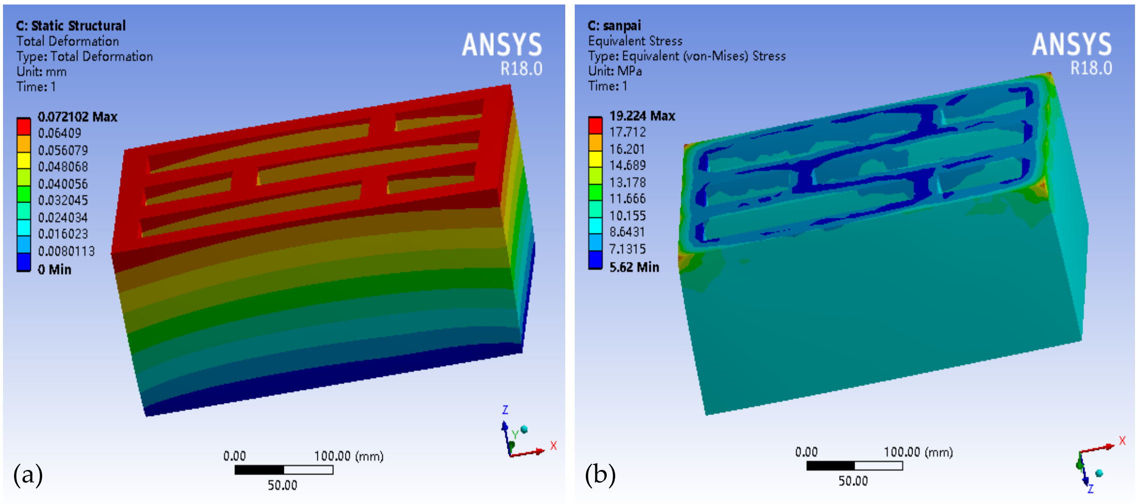

Figure 13. (**a**) Deformation contour plot; (**b**) von Mises equivalent stress contour plot.

Table 6. Simulation results of the von Mises equivalent stress.

Number	Number of Hole Rows	Hole Ratio %	Maximum von Mises Equivalent Stress /MPa	Minimum von Mises Equivalent Stress /MPa	Average von Mises Equivalent Stress /MPa
A_1	Three rows	44.4	19.22	5.62	9.553
A_2		42.4	18.70	5.59	9.559
B_1	Four rows	45.8	18.81	5.73	9.517
B_2		41.7	19.27	5.64	9.524
C_1	Five rows	43.8	18.80	5.67	9.496
C_2		42.9	18.78	5.67	9.502

Figure 13a presents that a large deformation at the edge of the block due to the principal stresses acted on it. Figure 13b shows that the minimum von Mises equivalent stress appeared in the cross ribs and inner wall of the block. The maximum von Mises equivalent stress appeared at the corners of the block (stress concentration area), and the area where stress concentration occurred was small. In summary, in this study, the maximum von Mises equivalent stress had no decisive influence on the overall bearing capacity and stability of the member.

Table 6 indicates that the average von Mises equivalent stress tended to decrease with the increase in the hole ratio when the hole shape and number of hole rows were fixed. The main reason was that the thickness of the middle rib of the block decreased with the increase in the hole ratio when the hole shape and the number of hole rows were constant. This reduced the compressive performance and connectivity between the concrete rib and wall of the block, thereby leading to a decrease in the average von Mises equivalent stress of the block.

3.2. Determination of Optimal AASCCIBs

According to Formula (19) and Table 3, judgment matrix A was obtained:

$$A = \begin{pmatrix} 1 & 2 & 3 \\ \frac{1}{2} & 1 & 2 \\ \frac{1}{3} & \frac{1}{2} & 1 \end{pmatrix} \quad (66)$$

Based on Formulas (20) and (21), $\lambda_{\max}$ and CI were 3.092 and 0.0046, respectively. According to reference [49], RI was 0.58. Based on Formula (22), CR was 0.0089. As CR was below 0.1, judgment matrix A satisfied the consistency test.

Matrix A was transformed to obtain the ranking weight vector ω (ω = (0.539 0.297 0.164)^T). Thus, the percentages of thermal, mechanical, and economic performances that affected the comprehensive performance of the AASCCIB were 53.9%, 29.7%, and 16.4%, respectively.

The heat transfer coefficient, Mises equivalent stress, and porosity were transformed to dimensionless using the normalization method. The results are listed in Table 7. The weighted comprehensive value of AASCCIBs was obtained by Formula (18). The results are presented in Figure 14.

Table 7. Dimensionless calculation results of each influence factor.

Number	Number of Hole Rows	Heat Transfer Coefficient	Equivalent Stress	Hole Ratio
A_1	Three rows	0.168	0.1671	0.170
A_2		0.170	0.1673	0.162
B_1	Four rows	0.163	0.1665	0.175
B_2		0.173	0.1666	0.160
C_1	Five rows	0.162	0.1662	0.168
C_2		0.164	0.1663	0.164

Note: A smaller heat transfer coefficient indicates better thermal performance. Therefore, the dimensionless value of the heat transfer coefficient was multiplied by -1 [44], to make the monotonicity of the three sub-factor functions of heat transfer coefficient, equivalent stress, and hole ratio consistent.

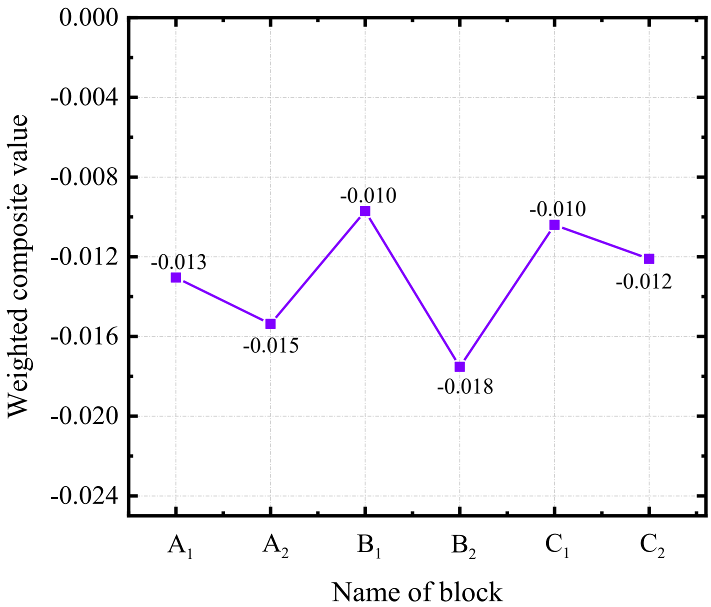

Figure 14. Weighted comprehensive value of each AASCCIB.

Figure 14 shows that the weighted comprehensive value of AASCCIB B_1 was largest. Thus, compared with several other AASCCIBs, AASCCIB B_1 had the optimal comprehensive performance. Therefore, AASCCIB B_1 was chosen to build the wall in the following modeling. The heat transfer coefficient and average von Mises equivalent stress of AASCCIB B_1 were 0.446 W/(m^2·K) and 9.52 MPa, respectively.

3.3. Improvement Effect of AASCCIB Wall on the Indoor Thermal Environment

Through the ANSYS CFX simulation, the indoor temperature changes of the building with the OB wall and building with the AASCCIB wall were informed. China is located in the northern hemisphere of the Earth. The day with the shortest sunshine time and the lowest solar altitude angle is the winter solstice. From the perspective of passive heat collection, the amount of solar radiation on this day is the lowest of the year. On the contrary, the summer solstice is the day with the longest sunshine time and the highest solar altitude angle, i.e., the solar radiation on this day is the highest in the year. Therefore, in the simulation analysis of the thermal insulation performance of the wall, the winter solstice (summer solstice) was selected as the date of the outdoor boundary condition. In addition, the indoor temperature of the room with the worst thermal comfort on the first floor (second floor) was used as the temperature of the first floor (second floor) in this study. The simulation results are presented in Figure 15.

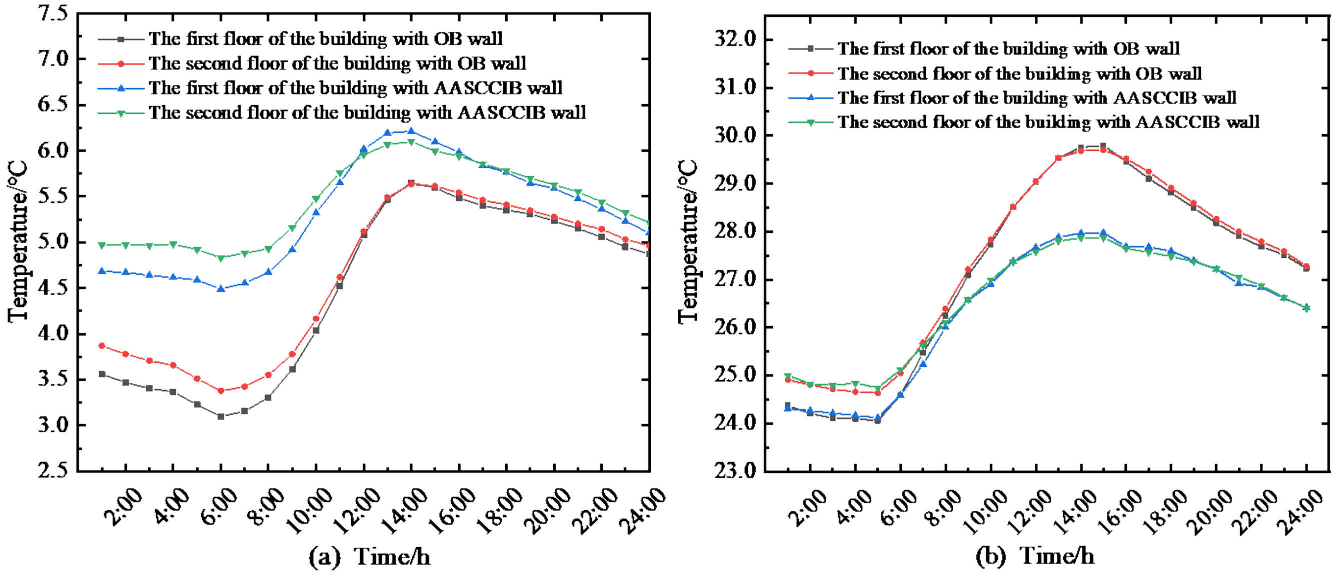

Figure 15. Indoor temperature of the building. (**a**) On the winter solstice; (**b**) on the summer solstice.

As shown in Figure 15a, the indoor temperatures of the rooms on the first and second floors of the building with the OB wall were lowest at 6:00 and highest at 14:00. The indoor lowest, highest, and average temperatures of the room on the first floor were 3.10, 5.65, and 4.47 °C, respectively. The indoor lowest, highest, and average temperatures of the room on the second floor were 3.37, 5.63, and 4.61 °C, respectively. For the building with the AASCCIB wall, the indoor temperatures of the rooms on the first and second floors were lowest at 6:00 and highest at 14:00. The indoor lowest, highest, and average temperatures of the room on the first floor were 4.49, 6.21, and 5.31 °C, respectively. The indoor lowest, highest, and average temperatures of the room on the second floor were 4.83, 6.10, and 5.43 °C, respectively. Compared with the indoor lowest and average temperatures of the building with the OB wall, those of the building with AASCCIB walls increased by at least 1.39 and 0.82 °C. In addition, the indoor temperature difference decreased by at least 0.83 °C.

Figure 15b shows that the indoor temperatures of the rooms on the first and second floors of the building with the OB wall were lowest at 5:00, 24.06, and 24.64 °C, respectively. The indoor temperatures of the rooms on the first and second floors were highest at 17:00, 29.89, and 29.81 °C, respectively. The average indoor temperatures of the rooms on the first and second floors were 27.37 and 27.54 °C, respectively. For the building with the AASCCIB wall, the indoor temperatures of the rooms on the first and second floors were lowest at 5:00, 24.11, and 24.75 °C, respectively. The indoor temperatures of the rooms on the first and second floors were highest at 15:00, 28.14, and 28.03 °C, respectively. The average indoor temperatures of the rooms on the first and second floors were 26.58 and 26.70 °C, respectively. Compared with the indoor highest temperature of the building with the OB wall, that of the building with the AASCCIB wall decreased by at least 1.75 °C. The indoor average temperature and temperature difference decreased by at least 0.79 and 1.89 °C, respectively.

In summary, the indoor thermal environment of the building with AASCCIB walls was significantly improved compared to that of the building with the OB wall. This was manifested by the increase in the indoor lowest and average temperatures on the winter solstice. The indoor temperature difference decreased. On the summer solstice, the indoor highest temperature, average temperature. and temperature difference decreased.

4. Conclusions and outlook

In this study, six types of AASCCIBs with different internal structures were designed. Based on the FEM, the thermal and mechanical performances of the six AASCCIBs were simulated using ANSYS CFX. The AASCCIB with the optimal comprehensive performance was determined through multi-objective optimization. The improvement effect of the AASCCIB wall on the indoor thermal environment relative to the OB wall was quantitatively analyzed using ANSYS CFX. The conclusions of this study can be summarized as follows:

1. The von Mises equivalent stress and heat transfer coefficient of the AASCCIB decreased with the increase in hole ratio when the hole shape and number of hole rows were constant.
2. AASCCIB B_1 had the optimal comprehensive performance among the six AASCCIBs. The heat transfer coefficient and average von Mises equivalent stress of AASCCIB B_1 were 0.446 W/(m^2·K) and 9.52 MPa, respectively.
3. Compared with the indoor lowest and average temperatures of the building with the OB wall, those of the building with the AASCCIB wall increased by at least 1.39 and 0.82 °C on the winter solstice, respectively. The indoor temperature difference decreased by at least 0.83 °C. In addition, the indoor highest temperature, average temperature, and temperature difference decreased by at least 1.75, 0.79, and 1.89 °C on the summer solstice, respectively.

This study quantitatively elucidated the improvement effect of the AASCCIB walls on the indoor thermal environment relative to the OB walls. However, the positive effect of the AASCCIB walls on the building energy consumption was unclear. To promote the development of wall materials and building energy efficiency, the reduction effect of the AASCCIB wall on the building energy consumption will be quantitatively analyzed in a follow-up study.

Author Contributions: Funding acquisition, Y.Z.; Methodology, X.F., Y.G., and Q.Z.; Software, X.F., Y.G., and Q.Z.; Writing—original draft, X.F. and Y.G.; Data curation, X.F. All authors have read and agreed to the published version of the manuscript.

Funding: This research was supported by the National Natural Science Foundation of China (grant no. 52078419 and 51678483).

Institutional Review Board Statement: Not applicable.

Informed Consent Statement: Not applicable.

Data Availability Statement: Not applicable.

Conflicts of Interest: The authors declare no conflict of interest.

References

1. Li, Y.; He, J. Evaluating the improvement effect of low-energy strategies on the summer indoor thermal environment and cooling energy consumption in a library building: A case study in a hot-humid and less-windy city of China. In *Building Simulation*; Tsinghua University Press: Beijing, China, 2021; Volume 14, pp. 1423–1437.
2. Ujanová, P.; Rychtáriková, M.; Mayor, T.S.; Hyder, A. A Healthy, Energy-Efficient and Comfortable Indoor Environment, a Review. *Energies* **2019**, *12*, 1414.
3. Ahn, J. Improvement of the Performance Balance between Thermal Comfort and Energy Use for a Building Space in the Mid-Spring Season. *Sustainability* **2020**, *12*, 9667.
4. Zhu, Y.Y.; Fan, X.N.; Wang, C.J.; Sang, G.C. Analysis of Heat Transfer and Thermal Environment in a Rural Residential Building for Addressing Energy Poverty. *Appl. Sci.* **2018**, *8*, 2077.
5. Kalua, A. Urban Residential Building Energy Consumption by End-Use in Malawi. *Buildings* **2020**, *10*, 31.
6. Xu, X.; Mumford, T.; Zou, P. Life-cycle building information modelling (BIM) engaged framework for improving building energy performance. *Energy Build.* **2020**, *231*, 110496.
7. Alsheyab, M. Recycling of construction and demolition waste and its impact on climate change and sustainable development. *Int. J. Environ. Sci. Technol.* **2021**, *1*, 1–10.
8. Liu, H.W.; Li, J.; Su, Y.F.; Wang, Y.S. Estimation Method of Carbon Emissions in the Embodied Phase of Low Carbon Building. *Adv. Civ. Eng.* **2020**, *2020*, 8853536.
9. Li, R.Y.; Li, Y.Y. Discussion on the innovation of new wall materials. *Charming China* **2014**, *22*, 263.
10. Li, P.; Sun, D.S.; Ding, Y.; Wang, A.G. Thermal Testing and Simulation of Self-thermal Insulation Block. *China Concr. Cem. Pro.* **2015**, *8*, 63–66.
11. Jiao, Z.; Wang, Y.; Zheng, W.; Huang, W.; Zhou, X. Use of Industrial Waste Slag in Alkali-Activated Slag Ceramsite Concrete Hollow Blocks. *Appl. Sci.* **2018**, *8*, 2358.
12. Rashad, A.M. Recycled waste glass as fine aggregate replacement in cementitious materials based on Portland cement. *Constr. Build. Mater.* **2014**, *72*, 340–357.
13. Imbabi, M.; Carrigan, C.; Mckenna, S. Trends and developments in green cement and concrete technology. *Int. J. Sustain. Built Environ.* **2012**, *1*, 194–216.
14. Awoyera, P.; Adesina, A. A critical review on application of alkali activated slag as a sustainable composite binder. *Case Studies Constr. Mater.* **2019**, *11*, e00268.
15. Rodríguez, E.D.; Mejia, R.; Puertas, F. Alternative concrete based on alkali-activated slag. *Mater. Constr.* **2008**, *58*, 53–67.
16. Liu, S.X.; Shen, L.L.; Niu, F.S. Researching Status and Prospect of Lightweight Aggregates Obtained from Solid Wastes in China. *Adv. Mater. Res.* **2011**, *163–167*, 624–628.
17. Xie, J.; Liu, J.; Liu, F.; Wang, J.; Huang, P. Investigation of a new lightweight green concrete containing sludge ceramsite and recycled fine aggregates. *J. Clean. Prod.* **2019**, *235*, 1240–1254.
18. Li, M.; Zhou, D.Y.; Jiang, Y.Q. Preparation and Thermal Storage Performance of Phase Change Ceramsite Sand and Thermal Storage Light-weight Concrete. *Renew. Energy* **2021**, *175*, 143–152.
19. Sang, G.C.; Du, X.Y.; Zhang, Y.K.; Zhao, C.Y.; Cui, X.L.; Cui, H.Z.; Zhang, L.; Zhu, Y.Y.; Guo, T. A novel composite for thermal energy storage from alumina hollow sphere/paraffin and alkali-activated slag. *Ceram. Int.* **2021**, *47*, 15947.
20. Akgul, B.A.; Karapınar, E. Investigation and Evaluation of Thermal Analysis for Different Wall Structures with Finite Element Method, Simulation of Temperature Distribution and Reaction in the Wall Types. *Euro. J. Math. Eng. Nat. Med. Sci.* **2021**, *8*, 132–144.
21. Ait-Taleb, T.; Abdelbaki, A.; Zrikem, Z. Simulation of coupled heat transfers in a hollow tile with two vertical and three horizontal uniform rectangular cavities heated from below or above. *Energy Build.* **2014**, *84*, 628–632.
22. Boukendil, M.; Abdelbaki, A.; Zrikem, Z. Simulation of the temperature field for massive concrete structures using an interval finite element method. *Eng. Comput.* **2020**, *37*, 2467–2486.
23. Hawkes, P.W.; Kasper, E. 11-The Finite-Difference Method (FDM). *Principl. Electr. Opt.* **1996**, *116*, 159–174.
24. Mazumder, S. The Finite Difference Method—ScienceDirect. *Numer. Methods Partial Differ. Equ.* **2016**, *12*, 51–101.
25. Cheng, Y.M.; Bai, F.N.; Peng, M.J. A novel interpolating element-free Galerkin (IEFG) method for two-dimensional elastoplasticity. *Appl. Math. Model.* **2014**, *38*, 5187–5197.
26. Mukherjee, S.; Liu, Y. The Boundary Element Method. *Int. J. Comp. Meth-Sing*. **2013**, *10*, 1350037.
27. Mazumder, S. The Finite Volume Method (FVM). *Numer. Meth. Part. Differ. Equ.* **2016**, *1*, 277–338.
28. Teng, C.; Yang, Q.; Peng, H. Numerical Thermal Optimization of the Hole Structures of Pottery Grain Concrete Hollow Blocks. *Mater. Rev*. **2011**, *25*, 280-284.
29. Gao, H.; Wei, G. Complex Variable Meshless Manifold Method for Transient Heat Conduction Problems. *Int. J. Appl. Mech.* **2017**, *9*, 1750067.

30. Gao, H.; Wei, G. Numerical solution of Potential Problems using Radial Basis Reproducing Kernel Particle Method. *Results Phys.* **2019**, *13*, 102122.
31. Muttalli, R.S.; Agrawal, S.; Warudkar, H. CFD Simulation of Centrifugal Pump Impeller Using ANSYS-CFX. *Int. J. Innov. Res. Sci. Eng. Technol.* **2014**, *3*, 15553–15561.
32. MOHURD. *Self-Insulation Concrete Compound Blocks: JG/T 407-2013*; China Architecture Building Press: Beijing, China, 2013.
33. Zheng, J.S.; Zhang, G.Z. Design and heat transfer performance of warming compound blocks with slag concrete. *New Build. Mater.* **2012**, *39*, 63–65.
34. Bathe, K.J. *Finite Element Procedures*; Prentice-Hall: Hoboken, NJ, USA, 2006.
35. Sardari, P.T.; Mohammed, H.I.; Mahdi, J.M.; Ghalambaz, M.; Gillott, M.; Walker, G.S.; Grant, D.; Giddings, D. Localized heating element distribution in composite metal foam-phase change material: Fourier's law and creeping flow effects. *Int. J. Energy Res*. **2021**, *45*, 13380–13396.
36. Pankaj; Arif, M.; Kaushik, S.K. Convexity studies of two anisotropic yield criteria in principal stress space. *Eng. Comput.* **1999**, *16*, 215–229.
37. Li, Q.; Steven, G.P.; Xie, Y.M. On equivalence between stress criterion and stiffness criterion in evolutionary structural optimization. *Struct. Optim.* **1999**, *18*, 67–73.
38. Pazera, E. Heat Transfer in Periodically Laminated Structures-Third Type Boundary Conditions. *Int. J. Comput. Meth.* **2021**, *18*, 2041011.
39. MOHURD. *Code for Thermal Design of Civil Building: CB50176-2016*; China Architecture Building Press: Beijing, China, 2016.
40. MOHURD. *Design Standard for Energy Efficiency of Rural Residential Buildings: GB50176-2016*; China Architecture Building Press: Beijing, China, 2016.
41. MOHURD. *Design Standards for Energy Efficiency of Residential Buildings in Hot Summer and Cold Winter Zones: JGJ134-2010*; China Architecture Building Press: Beijing, China, 2010.
42. Sánchez-Zarco, X.G.; González-Bravo, R.; Ponce-Ortega, J.M. Multi-objective Optimization Approach to Meet Water, Energy, and Food Needs in an Arid Region Involving Security Assessment. *ACS Sustain. Chem. Eng.* **2021**, *9*, 4771–4790.
43. Hamka, M.; Harjono, H. Application of fuzzy preference relations method in AHP to improve judgment matrix consistency. In *IOP Conference Series: Materials Science and Engineering*; IOP Publishing: Bristol, UK, 2020; Volume 821, p. 12035.
44. Yang, Z.T.; Liu, Y.; Yin, G.S.; Shi, M.H.; Wei, P.F. Optimization design and analysis of multi-row ceramsite concrete composite block structure. *Bull. Chin. Ceram. Soc.* **2020**, *39*, 113–123.
45. Zhao, Q.; Fan, X.N.; Wang, Q.; Sang, G.C.; Zhu, Y.Y. Research on Energy-Saving Design of Rural Building Wall in Qinba Mountains Based on Uniform Radiation Field. *Math. Probl. Eng.* **2020**, *2020*, 9786895.
46. Chandrupatla, T.R.; Belegundu, A.D. *Introduction to Finite Element in Engineering*; Prentice-Hall: Hoboken, NJ, USA, 1991.
47. Zhang, Q.Y.; Huang, J. *Standard Meteorological Database Used for Buildings in China*. Mechanical Industry Press: Beijing, China, 2004.
48. Samoshkin, S.L.; Meyster, A.O.; Yukhnevskiy, M.A. Methodical issues of determination of the average heat transfer coefficient of the passenger car body. *Vest. Rail. Res. Ins.* **2020**, *78*, 344–350.
49. Guo, T.M.; Hu, S.T.; Liu, G.D. Evaluation Model of Specific Indoor Environment Overall Comfort Based on Effective-Function Method. *Energies* **2017**, *10*, 1634.